



City Research Online

City, University of London Institutional Repository

Citation: Unal, G. B., Nain, D., Slabaugh, G. G. & Fang, T. (2011). Generating shapes by analogies: An application to hearing aid design. *Computer-Aided Design*, 43, pp. 47-56. doi: 10.1016/j.cad.2010.09.008

This is the accepted version of the paper.

This version of the publication may differ from the final published version.

Permanent repository link: <https://openaccess.city.ac.uk/id/eprint/4694/>

Link to published version: <https://doi.org/10.1016/j.cad.2010.09.008>

Copyright: City Research Online aims to make research outputs of City, University of London available to a wider audience. Copyright and Moral Rights remain with the author(s) and/or copyright holders. URLs from City Research Online may be freely distributed and linked to.

Reuse: Copies of full items can be used for personal research or study, educational, or not-for-profit purposes without prior permission or charge. Provided that the authors, title and full bibliographic details are credited, a hyperlink and/or URL is given for the original metadata page and the content is not changed in any way.

Generating Shapes by Analogies: An application to Hearing Aid Design

Gozde Unal^{a,1,2}, Delphine Nain^b, Greg Slabaugh^c, Tong Fang^{d,2}

^a*Sabanci University, Faculty of Engineering and Natural Sciences, Istanbul, Turkey*

^b*McKinsey and Company, Boston, MA, USA*

^c*MedicSight, London, UK*

^d*Siemens Corporate Research, Princeton, NJ, USA*

Abstract

3D shape modeling is a crucial component of rapid prototyping systems that customize shapes of implants and prosthetic devices to a patient's anatomy. In this paper, we present a solution to the problem of customized 3D shape modeling using a statistical shape analysis framework. We design a novel method to learn the relationship between two classes of shapes, which are related by certain operations or transformation. The two associated shape classes are represented in a lower dimensional manifold, and the reduced set of parameters obtained in this subspace is utilized in an estimation, which is exemplified by a multivariate regression in this paper. We demonstrate our method with a felicitous application to estimation of customized hearing aid devices.

Keywords: Shape estimation, shape regression, customized shape modeling, statistical shape modeling, hearing aid design

¹Email: gozdeunal@sabanciuniv.edu, URL: <http://vpa.sabanciuniv.edu/people/gozdeunal/>
Address: Sabanci University, Faculty of Engineering and Natural Sciences, Istanbul, Turkey, Tel:+90-216-483-9553, Fax:+90-216-483-9550.

²This work is supported by Siemens Corporate Research, Princeton NJ, USA.

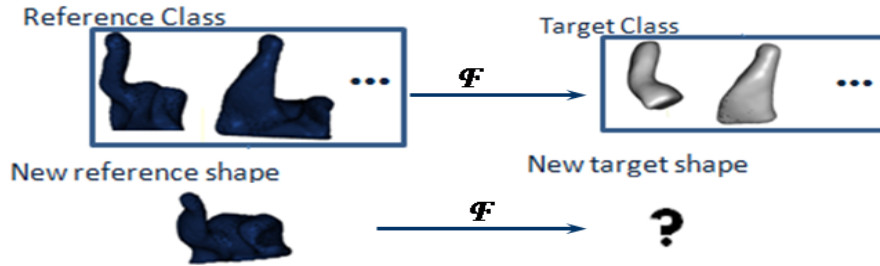


Figure 1: Exemplified Shape Estimation Problem.

1. Introduction

3D shape modeling and estimation is a crucial task in custom design of anatomical shapes. A sample shape estimation problem in rapid prototyping of hearing aid devices is depicted in Figure 1. For a comfortable fit, it is important that the shape of the hearing aid matches the patient’s ear geometry. The two classes of shapes, here patients’ 3D raw ear impressions and the output hearing aid shapes, are normally related by certain operations or a transformation \mathcal{F} . Current practice involves mainly a manual design even with a recent transfer of this process to a CAD environment. The goal of this work is to automate the process of hearing aid shell design and similar other prosthetic part design for increasing patient comfort, efficiency, repeatability, and throughput in customized rapid prototyping systems.

1.1. Related Work

Our approach to solve this problem is to resort to an arsenal of shape learning tools from the celebrated statistical shape theory (Kendall [1], Bookstein [2], Dryden and Mardia [3], Cootes and Taylor [4] et al.). The classical

Bookstein shape representation entails removing the translation, rotation, and scale, and what remains constitute the interesting geometric properties of a shape. After such a pre-alignment of shapes to a common coordinate space, the structure of the shape variability can be investigated for instance through a covariance analysis, and the principal components (PCs) can be computed to obtain the modes of variation around a mean prototypical shape.

One of the first applications of PC analysis (PCA) to images was presented by Turk and Pentland [23] to model faces in a reduced PC space for face recognition. In [6], a statistical shape model was built for the human ear canal (as point clouds), where the correspondences were obtained by warping a template onto shapes, which are annotated with 18 landmarks by a specialist. In [7] a smoother dense mesh was obtained by a Markov field regularization of the correspondence field. In these works, the ear canal model is used for analysis of gender differences in its shape, and for its deformation by mandibular movement [8]. Manual marking of landmarks is not suitable for rapid prototyping systems, moreover, finding stable feature points in all shapes is difficult due to individual variations. The correspondence problem was alleviated in an Eulerian shape representation via signed distance functions (SDFs) in [9] that used PCA, which we also follow in this work. It is known that the SDFs do not form a vector space, and the PCA will not necessarily result in SDFs in the 3D embedding space. However, the 3D shape surfaces are on a 2D manifold, and only the zero level sets of their SDFs contain the desired shape information, hence the analysis such as PCA will still be valid as evidenced by the previous art [9]. A shape prior was built to guide the segmentation of objects in images in [9], which is different from

our problem. Variations on PCA such as kernel PCA [10, 11] and principal factor analysis [12] were employed for statistical shape analysis, although PCA is preferred in our work for its optimality in dimensionality reduction. In a recent work [13], regression techniques are utilized to investigate degrees of correlation and dependence variation between shapes of different structures within the brain. Our method is different in mathematical details and includes deformation of predicted shapes via predicted difference shapes and fitted planes, with a focus on shape generation for prosthetic devices. In [14], Fréchet expectation was used to generalize univariate regression to manifold-valued data to study the effect of aging on brain shape in patient populations.

Another related body of work exists in computer graphics. For instance, in SCAPE [24], given a sparse representation such as a partial view over a human body, a method to obtain a complete mesh model of the body is presented. In addition, given marker motion capture data, a full 3D animation of a moving person is produced. Separate models of body deformation for pose and body shape changes in humans are learned in a reduced PC space. Similarly, in Allen et al’s work [25], a dense mesh is fitted to a sparse marker data for various applications such as creating hole-free surfaces, and synthesizing new human body shapes using PC modes. The latter application is quite interesting as human features such as height, and weight of an individual are correlated with its principal components, and this relation is used to generate a new individual with prescribed features, e.g. a given height and weight. The idea resembles our work, however, rather than directly relating features, which are not readily available, to its shape representation,

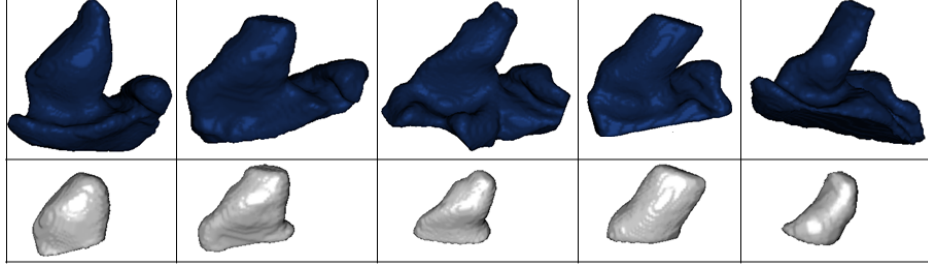


Figure 2: Each shape from the target class (gray) on the second row are related to the reference shapes (dark blue) on the first row by a certain transformation.

we directly relate the two corresponding anatomical shapes of an individual, which are tied to each other through a hearing aid designing process.

Our work is also similar in spirit to the image analogy problem [5], where a new painting D is produced by the input photograph C, by copying matching patches from a prior painting/photo pair A/B. The explicit relation between the pairs is not learned however, which is our aim in this work.

1.2. Our Contribution

Our main contribution is the development of an automatic shape transformation method to be used in various applications like customized design of anatomical parts. We first introduce our shape estimation methodology following a felicitous application to hearing aid design, in which a coupled pair of shapes are involved as shown in Figure 2. The shapes in the first class are the surface models of the raw ear impressions of patients, and the shapes in the second class are the related processed canal model into which the hearing aid components will be placed. The raw shapes are characterized by the ear canal (long and thin structure on the top) and the external ear

parts (round bowl-like structure in the bottom, called concha) [15], and the processed shapes, which we call as the target shapes, are characterized by mainly the canal geometry of the raw shapes.

As can be seen, these two shape classes are related to each other by certain operations, and the problem at hand is, without knowing the transformation between them and presented with an example set of shapes from the two classes, to be able to learn the relation between these two shape spaces explicitly. Our motivation is also tied to not having to resort to feature extraction, which often is more prone to errors with variations in the shape geometry. For instance, problems with aperture feature detection in ear impressions, were discussed in a feature-based alignment of ear canal models work of Zouhar et al [27].

We note that the approach by Kilian et.al [16], who utilized Riemannian metrics for both a rigid and an isometric deformation among shapes, would be an alternatively applicable approach for our problem. The geodesic paths in shape space with the devised metrics were computed to morph an initial or boundary value shape into a set of shapes that sample the continuous path in between the shapes. This would be quite useful if we already partitioned the given shape space into a set of prototypes, obtained from a principled and sufficiently narrow categorization of the shapes into meaningful clusters. One could use the computed geodesic path between a prototype source and target shape and then transfer the same deformation over the given shape to obtain the output shape.

Here, first, a transformation is learned to generate a target shape given a new shape from the first class. We investigate the structure of the shape

variability, through a covariance analysis, and the PCs are computed to obtain the modes of variation around the mean shape (Figure 3). We note that SDF shape representation is used in this work, and PCA is performed on the SDFs. One advantage of looking at PCs is that they can be geometrically interpreted in terms of shape characteristics [29]. For the raw shapes, the first three PCs account for 64.4% of the shape variability (the 4th PC accounting for 72.8%), respectively, and primarily involve enlargement towards external parts and canal expansion, widening and straightening vs. shrinkage and bending in general. For the target/processed shape class, the first three PCs account for 83.4% shape variability (the 4th PC accounting for 86.8%), measure similar effects. The 4th PCs measure an anisotropic scale (thinning at the center of the shape vs a widening). A typical discrete shape representation has on the order of 10^3 dimensions (e.g. a surface mesh with ~ 5000 vertices, or an SDF grid with 10^6 voxels), and from such analysis, one can see that the two shape classes, say \mathcal{R} , and \mathcal{T} , can be represented by their first several PCs, and this suggests a projection onto a low dimensional space spanned by these few PCs, say \mathcal{R}_p , and \mathcal{T}_p .

The idea here is that the higher order PCs usually account for local, smaller and nonlinear variations that can introduce noise into a global estimation, hence performing a shape estimation over a reduced dimensional manifold effectively filters out noise and outlier effects and generates an efficiently well-transformed shape as close as possible to the expected output shape geometry. This is as opposed to a higher sensitivity of feature-based methods to noise and variations in shapes, for instance as in extracting features to devise rules for a rule-based shape design.

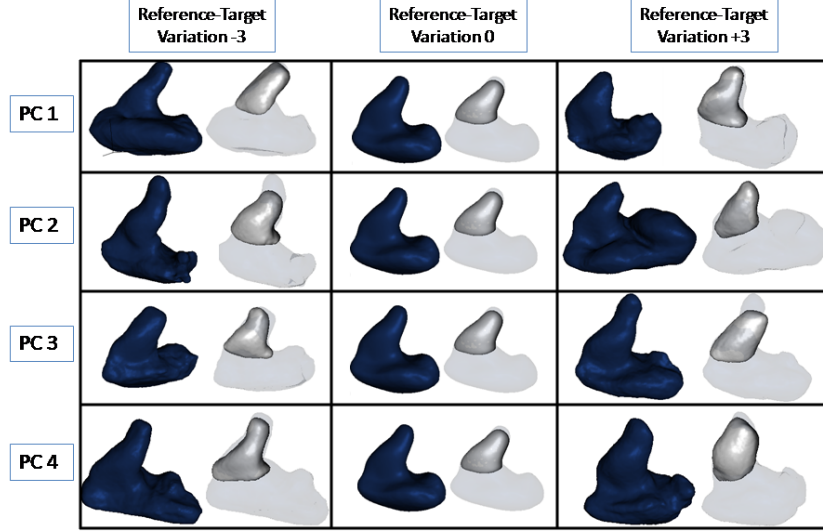


Figure 3: The first four principal components (PCs) and their variations around the mean (mean=0 variation) for both the reference and target shape spaces.

We can also view this analysis as the two related shape spaces modeled by Gaussian shape probability densities hence with only a mean prototypical shape together with its principal modes, i.e. the shape variations. Then a joint probability density could be written as:

$$P(\mathcal{R}, \mathcal{T}) = \frac{\exp(-\frac{1}{2}(\mathcal{R} - \mathbf{m}_R)^T \Sigma_R^{-1}(\mathcal{R} - \mathbf{m}_R) - \frac{1}{2}(\mathcal{T} - \mathbf{m}_T)^T \Sigma_T^{-1}(\mathcal{T} - \mathbf{m}_T))}{\sqrt{2\pi|\Sigma_R|}\sqrt{2\pi|\Sigma_T|}} \quad (1)$$

where \mathbf{m} are prototypical mean shapes for each class. If we further model the two shapes separately by their respective Gaussian probability densities, then what remains is two linear shape spaces independently represented. A likelihood probability for the target shape class can be written in this case simply as:

$$P(\mathcal{T}|\mathcal{R}) = \frac{\exp(-\frac{1}{2}(\mathcal{T} - \mathbf{m}_T)^T \Sigma_T^{-1}(\mathcal{T} - \mathbf{m}_T))}{\sqrt{2\pi|\Sigma_T|}} \quad (2)$$

Our main observation was that through the likelihood function, the main descriptor that characterizes each shape space, i.e. the covariance matrices, can be tied to each other ($\Sigma_T = \mathcal{F}^\Sigma \Sigma_R$) as we are interested in estimating a simple transformation \mathcal{F} to explain the relationship between the two shape classes: $\mathcal{F} \circ \mathcal{R}_p = \mathcal{T}_p$. An intuitive approach here is to carry out a multivariate regression analysis between the PCs to obtain a linear transformation between the two low dimensional shape spaces. Thus, the relationship between the two approximated shape spaces is incorporated into the multivariate regression formulation to introduce a coupling effect and to suppress most of the higher order variations and nonlinear effects. The estimated transformation matrix along with an auxiliary class of difference shapes introduced will provide a proof of concept for a desired shape estimation framework, and achieve a good performance.

Modeling of the relationship between two classes of shapes on a linear manifold will be described in Section 2 exemplified by the Hearing Aid Application. As a preprocessing we design a biased registration for shapes that significantly differ in geometry, as described in Section 2.2 followed by the shape estimation details in Section 2.3-2.5. The results are presented in Section 3 followed by conclusions and discussions in Section 4.

2. Shape Estimation for Hearing Aid Shell Rapid Prototyping

In this section, we explain the details of our general shape estimation methodology, exemplified on a particular rapid prototyping application, which is automatic estimation of the hearing aid shells from individual patient ear impression surfaces.

2.1. Data Description

The design process starts with a rough mold of the patient’s ear, so called undetailed shell (shape), that is then detailed by a specialist [17]. The detailing process includes cutting unused parts based on the desired shell style and the geometry of the patient’s mold (Fig 4), rounding edges and other operations needed to fit the electronics in the shell. This is a time-consuming process that is based on the skills and experience of the specialist. Alternatively, the specialist can carry out the detailing on digitized ear shells using CAD software systems, which are still not-fully automatic. The initial motivation of our work was to remove this bottleneck in rapid prototyping systems for hearing aid devices, however, these ideas can be applied to similar shape estimation problems.

In our learning approach, digitized undetailed ear molds and their corresponding manually detailed molds, the latter of which are used in training and validation and referred to as the ”Ground Truth” (GT) shapes, are acquired from a specialist. A 3D point cloud is obtained and triangulated to build a polygonal mesh surface, which is then transferred into an SDF representation. For conversion from a triangulated mesh to a voxelized SDF shape, the mesh is first placed over a fixed volumetric grid (e.g. a voxel grid of 100^3 in this work), so that inside and outside of the shape can be marked over the grid at each voxel. After placement over to the volumetric grid, the voxels over the shape surface are marked as zero, and distances from each voxel coordinate to the surface are computed utilizing fast marching [21]. To construct the SDF, finally, positive distances are used outside the shape and negative distances are used inside the shape.

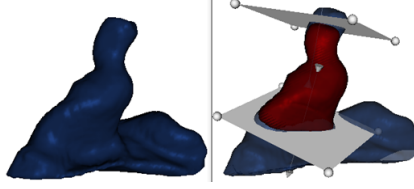


Figure 4: Ear impression: a typical raw (undetailed) shape (blue); target (detailed) shape with cutting planes (red).

2.2. Biased Shape Registration

For the method presented here, there are two shape alignment problems: (i) all the reference, i.e. undetailed, shapes in the data population should be aligned. This is needed to factor out rigid pose variations in a shape population to prevent their influence in the PC analysis. (ii) The undetailed shapes must be aligned with the corresponding target detailed shapes in order to compute an auxiliary difference shape, which will be used in further refinement of the shape estimated directly from the shape regression step.

Iterative closest point-ICP algorithms are widely used for automatic global rigid alignment [28]. Based on a variant of ICP, the rigid alignment of all the undetailed shapes were carried out by the method presented in [27] before they were converted to a voxelized signed distance transform representation. As a rigid transformation model, 3D rotation and 3D translation parameters were used, and each undetailed shape in the training set was first registered to an arbitrarily chosen undetailed shape in the set. After the first step, an average template shape was computed, and all the shapes were registered to the average shape. The groupwise registration of all undetailed shapes clearly will not perfectly align all of the undetailed ear impressions. However, as

pointed by Leventon *et al* [9], an SDF representation provides tolerance to slight misalignment of shape pose because even if there is slight misalignment between voxels of two shapes, their distance map values will still be highly correlated.

For the second alignment problem, we utilized a a variational approach, where, a rigid registration is typically based on a sum of squared distances cost between the two shapes, Φ^u and Φ^d :

$$E(g) = \int_{\Omega} \mathcal{X}_{\alpha}(\Phi^u(\mathbf{X}), \Phi^d(g(\mathbf{X}))) [\Phi^u(\mathbf{X}) - \Phi^d(g(\mathbf{X}))]^2 d\mathbf{X}. \quad (3)$$

Here, g is a rigid transformation $g(\mathbf{X}) = \mathbf{R}\mathbf{X} + \mathbf{T}$, $\mathbf{X} \in \mathbb{R}^3$, with parameters g_i of 3D rotation matrix \mathbf{R} , and 3D translation \mathbf{T} . Φ^u and Φ^d are the undetailed and detailed shell SDFs defined over the domain Ω . Here,

$$\mathcal{X}_{\alpha} = \begin{cases} 0, & \min(|\Phi^u|, |\Phi^d|) > \alpha \\ 1, & \min(|\Phi^u|, |\Phi^d|) < \alpha \end{cases} \quad (4)$$

is a characteristic function to take into account in the energy domain those points that are in a band around each shape, where the band radius α needs to be fixed according to the expected maximum distance between two shapes [18].

Applying the rigid registration with min indicator function (Eq.3-4) to our problem leads to failure in most cases as seen in Figure 5 b, e and h, even with "good" heuristic α parameter values. The reason is that the detailed shape Φ^d is significantly smaller than the undetailed shape, and parts of Φ^u that do not exist in the detailed shell still influence the registration. In order to avoid this problem, we use a "biased" energy in a similar variational formulation. We propose a modified indicator function with a distance restricted to a band

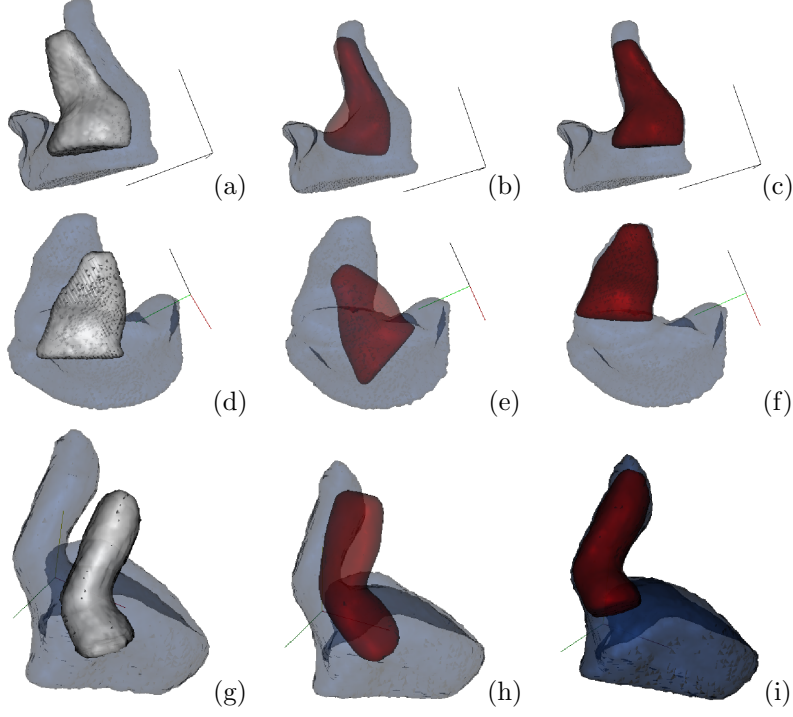


Figure 5: Registration of detailed ear impressions to undetailed: (a,d,g) shapes before registration; (b,e,h) shape (red) after original registration; (c,f,i) shape (red) after biased registration by Eq.(6).

around both Φ^d and Φ^u , but constrained mainly by the smaller of the two shapes:

$$\mathcal{X}_\beta(\Phi^u, \Phi^d) = \begin{cases} 0, & \max(|\Phi^u|, |\Phi^d|) > \beta \\ 1, & \max(|\Phi^u|, |\Phi^d|) < \beta \end{cases} \quad (5)$$

Deriving the energy functional with the max indicator function, we obtain the corresponding biased rigid registration equation:

$$\begin{aligned} \frac{\partial g_i}{\partial t} = & \int_{\Omega} \mathcal{X}_\beta(\Phi^u(\mathbf{X}), \Phi^d(g(\mathbf{X}))) [\Phi^u(\mathbf{X}) - \Phi^d(g(\mathbf{X}))] \\ & \left\langle \nabla \Phi^d(g\mathbf{X}), \frac{\partial g(\mathbf{X})}{\partial g_i} \right\rangle d\mathbf{X} \end{aligned} \quad (6)$$

where t is an iteration parameter to update the registration parameters g_i , and $\langle \cdot, \cdot \rangle$ indicates the inner product operation in \mathbb{R}^3 . Figure 5 depicts results in ear shell registration, where the biased alignment was successful in (c), (f), and (i). We note that our biased registration idea resembles another variant of ICP-based registration for point cloud alignment by [26]. In that work, corresponding point pairs were rejected based on a maximum distance threshold between the points. Our biased registration incorporates the same idea into an energy between shapes represented by SDFs, and achieves the same desired constraint in a different setting.

2.3. Shape Regression

After alignment of the shapes, i.e. their SDFs, a covariance analysis is carried out over Σ_R and Σ_T separately, and the PCs are computed respectively. The shapes are projected onto a lower dimensional linear manifold via projection matrices P^R and P^T formed with a handful of PCs. For instance, the number of modes needed to explain 97% of the variability in the data resulted in a dimension $k = 19$, which is the number of PCs retained. On this reduced space, an explicit mapping between the undetailed and the detailed shape spaces is sought. With N undetailed training shapes, each was represented by its weights, $\mathcal{R}_p = \mathbf{w}^u = P^R(\mathcal{R} - \mathbf{m}_R)$, with $\mathcal{R} = \Phi^u$. Then the $N \times k$ weight matrix \mathbf{W}^u is formed whose i th row is the vector \mathbf{w}_i^u representing the i th undetailed shape. Similarly, \mathbf{W}^d represents the weight matrix for the projected detailed shapes \mathcal{T}_p 's. We would like to find a model that best describes the relation between the two shape classes in this highly reduced dimensional space, i.e., a mapping \mathcal{F} between the two shape

representations as:

$$\mathcal{F} \circ \mathbf{W}^u = \mathbf{W}^d. \quad (7)$$

The nature of the mapping depends on the complexity of the transformation sought. As expected, not all PC combinations will provide linear relations. Nonlinear local variations between the shapes show up for higher order PCs, which are the eigen shapes whose eigen values are smaller than the largest k eigen values. Although one could opt for sophisticated mappings between the two shape spaces, a linear relationship between the reduced representation of the two classes of shapes is chosen in order to mitigate the uncertainties in the higher order local relations. As such, a lower dimensional space discards the higher order and nonlinear variations of the shapes, and facilitates a linear relationship. In order to find a general multivariate regression between all the modes, we construct a linear least squares optimization problem:

$$\mathbf{W}^u \mathbf{F}^d = \mathbf{W}^d \quad (8)$$

where \mathbf{F}^d is a transformation matrix that *"encodes the detailing process"*: it transforms the undetailed shape class into the detailed shape class. The solution to this regression problem is simply given by:

$$\mathbf{F}^d = (\mathbf{W}^{u\ T} \mathbf{W}^u)^{-1} \mathbf{W}^{u\ T} \mathbf{W}^d \quad (9)$$

where \mathbf{W}^u , is of size $N \times k$, where $N > k$. Therefore, it is an overdetermined system, and the inverse of $\mathbf{W}^{u\ T} \mathbf{W}^u$ exists. It was inverted by an SVD decomposition [19] to obtain \mathbf{F}^d .

2.4. Auxiliary Shape Regression

For a customized design, the resulting detailed shell should conform exactly to the input patient data. A solution is to recover the ear canal geome-

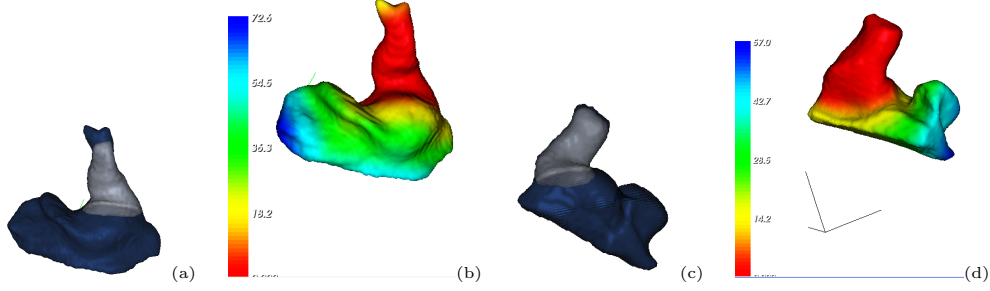


Figure 6: Two sample Aux shapes \mathbf{A}_i 's superimposed over the undetailed shapes in (b) and (d) obtained from the absolute difference of the pair of shapes: undetailed (dark blue) and the detailed GT (gray) rendered together in (a) and (c), respectively. The difference of the SDF values (hence unitless), is represented as a color map, where the lowest value, 0, is depicted by red color and increases towards blue.

try from the undetailed shell in between regions defined by the cutting planes, or practically the "cuts", performed by the specialist. For this purpose, we build a statistical model for a class of auxiliary shapes (Aux Shapes), to help deform the estimated model towards the patient ear canal anatomy as depicted in Figure 6. The Aux field \mathbf{A}_i are formed as the difference of shapes in the two training sets, i.e. $\Phi_i^u - \Phi_i^d$, and indicates where the two shapes match as expected after the input shape's modifications. In Fig. 6, it can be observed that the Aux shapes have mostly zero value in the canal region, and non-zero values in the top canal and concha regions.

Using each detailed/undetailed shape pair in the training set we obtain an aux field $\mathcal{A} = [\mathbf{A}_1, \dots, \mathbf{A}_N]$ on which we perform a covariance analysis to obtain a set of aux weights \mathbf{W}_i^a for each shape. We relate the aux weights and undetailed weights via:

$$\mathbf{W}^u \mathbf{F}^a = \mathbf{W}^a \quad (10)$$

and estimate \mathbf{F}^a through multivariate linear regression. In the end, along with the "detailing" transformation matrix \mathbf{F}^d , a second regression matrix \mathbf{F}^a is estimated to *"encode the crucial cutting operations of detailing"*.

2.5. Automatic Shape Generation

After the training phase, a new undetailed shape is given as input to the system, and the expected output is a corresponding detailed shell similar to one that would have been produced by a specialist. The flowchart in Figure 7 summarizes our automatic shape generation method: the new undetailed shape is registered to the mean shape from the training data as explained in Section 2.2. The weight vector for the new undetailed shape is computed by projection onto its PCs, then the weight vector for the detailed shape is estimated through multiplying it by the stored regression matrix in Eq.(9) to construct a regressed shape as in Fig 8-a. Next, aux shape weights are estimated via the regression matrix \mathbf{F}^a in Eq. (10) to construct \mathbf{A} . In Fig 8-b, the \mathbf{A} field is displayed over the regressed detailed shape.

2.5.1. Plane Estimation For Constraining Shapes

The regions of estimated \mathbf{A} that have non-zero distance values correspond to "cuts" that would have been made by the specialist. Those cuts usually produce flat surfaces. Since the estimated detailed shapes do not always have flat surfaces where the \mathbf{A} shape is non-zero, a clustering algorithm will be used to group points over the \mathbf{A} surface. First, we threshold the \mathbf{A} field to obtain a mask shape \mathbf{M} as follows:

$$\mathbf{M}(\mathbf{X}) = \begin{cases} 0, & \text{if } A(\mathbf{X}) > \text{maskCutOff} \\ 1, & \text{else} \end{cases}$$

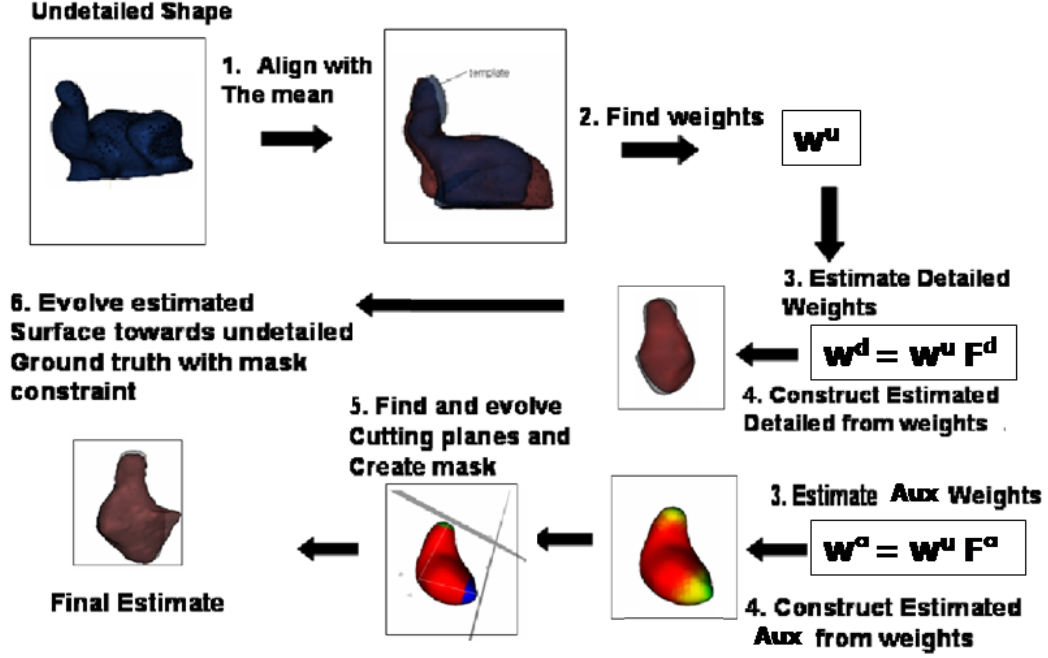


Figure 7: Flowchart describing the proposed automatic shape generation method.

Here, a typical value for the threshold: $maskCutOff = 1$, which is fixed for all the experiments. A point cloud is formed from the coordinates over the domain of the M shape: $X^c = \{X_i \text{ s.t. } M(X) = 0\}$, i.e. where M equals 0. Hence, the possible "cut" regions are collected in the constructed point cloud, which usually contains two sets of clustered points: one over the bottom of the canal and one over the tip of the canal regions. A noise reduction operation precedes the point cloud formation via two morphological operations, openings and closings to eliminate isolated points over the mask field M . Next, a k -means clustering algorithm is applied to the created point cloud with $k = 2$ clusters. Two separate planes are fitted to these clustered regions as shown in Figure 8-b3, where green and blue colored regions corre-

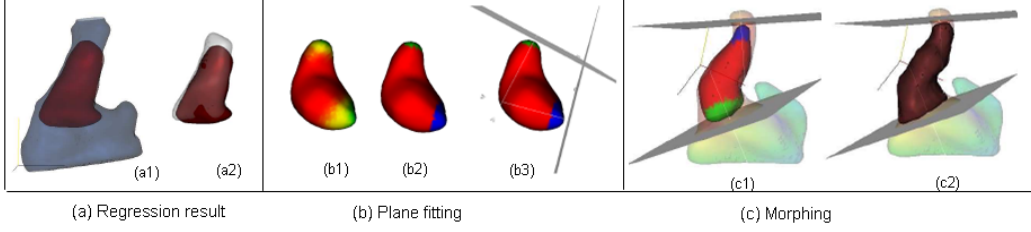


Figure 8: Detailed shape found through regression is depicted (in red/dark) on: (a1) the undetailed shape; (a2) the GT detailed shape (in grey/light). (b1) estimated Aux shape; (b2) the resulting clustering with 2 clusters; (b3) the fitted planes. Morph of an initial detailed surface (c1) towards the undetailed surface constrained by planes, final result (c2).

spond to the top and bottom "cut" regions. Each plane is represented by its normal \mathbf{N}^p and its distance to the origin, d . To fit a plane to a cluster of points $\mathbf{X}^c = [\mathbf{X}_0, \dots, \mathbf{X}_n]$ in a least-squares sense, we minimize the following sum:

$$E(\mathbf{N}^p, d) = \sum_{i=0}^n (\langle \mathbf{N}^p, \mathbf{X}_i \rangle - d)^2 \quad (11)$$

to estimate the plane normal \mathbf{N}^p and the location of its center d [20]. In the implementation, this can be achieved by using PCA of the point cloud, and choosing the two highest eigen value directions to define the plane tangent vectors and the smallest eigen value's eigen vector to define the plane normal.

Due to noise in clustered data points and estimation error, the fitted planes are sometimes not perfectly aligned with the surface of the estimated detailed shape Φ^d . In order to further align a fitted plane, we want to update the orientation of the plane to better match the orientation of the detailed shape surface near the plane. Therefore, to estimate a rotation matrix \mathbf{R}^j applied to the plane, we design an energy functional that will maximize the

global alignment between the rotated plane normal and the shape surface normal as follows:

$$E(\mathbf{R}^j) = \int_{\Omega^j} \langle \mathbf{R}^j \mathbf{N}^p(\mathbf{X}), \nabla \Phi^d(\mathbf{X}) \rangle d\mathbf{X}, \quad (12)$$

where Ω^j indicates either of the clustered regions at the top or bottom of the canal (e.g. the green and red colored regions in Figure 9), hence index $j \in \{t, b\}$. We maximize this energy via a variational approach by deriving it with respect to parameters of \mathbf{R}^j , and obtain the update equation for the rotation of the plane normal as:

$$\frac{\partial \mathbf{R}^j}{\partial t} = \int_{\Omega^j} \langle \nabla \Phi^d, \frac{\partial \mathbf{R}^j(\mathbf{X})}{\partial r_i^j} \mathbf{N}^p \rangle d\mathbf{X} \quad (13)$$

where r_i^j , ($i = 1, 2, 3$), are the rotation parameters of the plane, in an exponential coordinate representation of the 3D rotation. Two 3D rotations \mathbf{R}^j are estimated for both of the planes. We show sample plane evolutions in Figure 9 to illustrate the further correction on the orientation of the estimated plane via updates of the rotation parameters in Eq. (13). The corrected plane orientations with respect to the geometry of the shape can be observed.

2.5.2. Final Shape Morphing

After we estimate and correct the cutting planes in the detailing process, finally, we morph the regressed detailed shape, i.e. the result of regression in Eq.(9), completely towards the true patient geometry. The estimated planes form a new binary mask M^p to indicate the desired regions that drive the propagation of the estimated detailed shape towards the undetailed shell Φ^u , except at the parts that are detected as “cuts” with M^p . The final part of our algorithm involves a surface evolution by using the popular level set

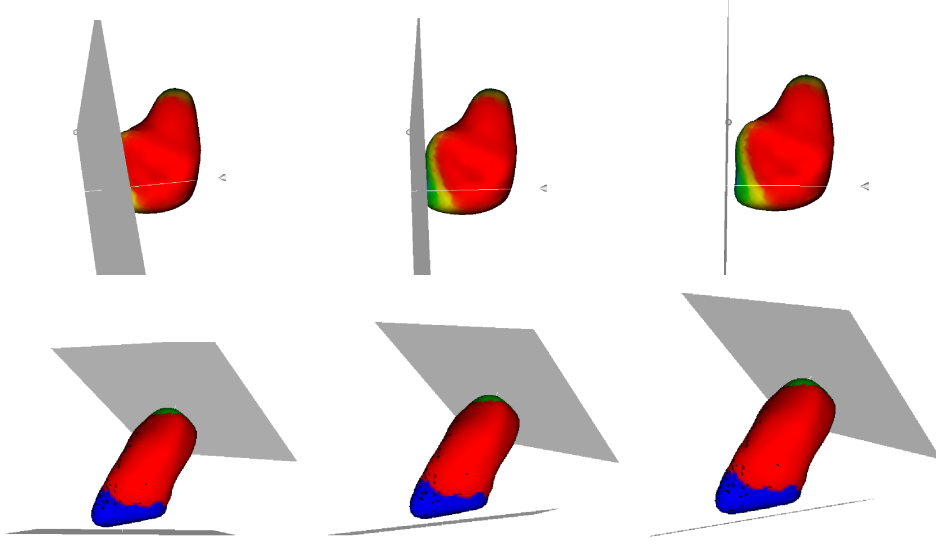


Figure 9: Sample plane evolutions for estimated detailed shapes: initial planes (left), after 2 iterations (middle), after 3 iterations (right). Color maps: (top) the continuous Aux field \mathbf{A} is shown, where red color represents low distances which increase towards green-yellow-blue colors; (bottom) after thresholding the Aux field to obtain a mask field \mathbf{M} , and k-means clustering, two clusters remain: here blue color indicates the canal bottom cluster, green color indicates the canal top cluster, and red color indicates the rest.

framework [21]. We define a partial differential equation (PDE) inspired by [22] for shape morphing modified by the plane mask M^p in our problem. The detailed surface is then deformed by the following PDE:

$$\frac{\partial \tilde{\Phi}^d(\mathbf{X})}{\partial t} = M^p(\mathbf{X})\Phi^u(\mathbf{X})|\nabla \tilde{\Phi}^d(\mathbf{X})| + \kappa(\mathbf{X})\nabla \tilde{\Phi}^d/|\nabla \tilde{\Phi}^d(\mathbf{X})| \quad (14)$$

with an initial condition Φ^d , which is the regression result, κ is the mean curvature over the surface, and $\tilde{\Phi}^d$ is the final shape generated as the output of our algorithm. Figure 8-c shows the morphing of the $\tilde{\Phi}^d$, driven by the sign of the Φ^u and continues to propagate until it reaches the planes via the mask $M^p(\mathbf{X})$ and flattens out.

3. Results

The hearing aid dataset utilized for the experiments includes 34 undetailed and the corresponding detailed shapes. Cross validation tests were performed as 34 leave-one-out experiments, where in each test, 33 of the shapes were used in the training and the remaining single shape was used in the testing phase. Table 1 presents average performance measures for these experiments. The Dice measure between two shapes A and B represented in the voxel domain is defined as $2\#(A \cap B)/(\#A + \#B)$, where $\#$ denotes the number of voxels on and inside a shape A. The average Dice measure and its standard deviation (std) between the GT, i.e. result of manual design, and the regressed detailed shells (result of Sec.2.3) show about $70 \pm 7\%$ overlap, which to a degree can justify using a linear transformation for relating undetailed and detailed shapes. The final deformed shapes showed $85 \pm 5\%$ overlap with the GT shape. The average absolute distance between the zero level sets of the ground truth and the estimated detailed shells for regressed shapes were $1.50 \pm 0.60\text{mm}$, whereas for the deformed final shape, it was $0.43 \pm 0.25\text{mm}$, which showed improved proximity. The manual design specifications allowed for maximum of 0.5mm error for a comfortable fit to patient’s anatomy. The maximum distance between the GT and estimated shapes were $5.0 \pm 1.7\text{mm}$ for the regressed result, and $3.6 \pm 0.9\text{mm}$ for the final shape. Although the specifications for manual design are set to 0.5mm, the errors are unexceptionally contained within the patient’s ear geometry by construction of the method, hence will not produce spiky or outward bulging shapes.

A popular method to compare two different studies is called the Bland-

Cross Validation/Average \pm Std	Regressed Shapes	Final Shapes
Dice measure (%)	70.76 ± 7.55	85.03 ± 5.69
Mean Absolute Distance (mm)	1.50 ± 0.60	0.43 ± 0.10
Max Absolute Distance (mm)	4.98 ± 1.72	3.59 ± 0.94

Table 1: Dice measure, Mean Absolute Distance, and the Maximum Absolute Distance between the estimated and the GT shapes for all 34 leave-one-out tests.

Altman method, which aims to measure consistency of the measurements [30]. The method states that for two clinical methods to be consistent, the average difference between the results of two measurements should be zero and that 95% of the difference should be less than two standard deviations. Figure 10 shows a scatter plot of the shape volume measurements resulting from the manual and automatic shape estimation. Most of the points are within two standard deviations which indicates that the manual and automatic results are consistent despite the fact that there is a consistent bias toward over-estimation of the target shape with the automatic method.

This is a natural outcome of the last step of our method in which the regressed shape deforms to the reference shape constrained by both the two estimated cut planes and the reference shape. However, this over-estimation, without exception occurs at the cut regions, and still fits inside the patient anatomy as depicted by color maps of distances to the GT shapes in Figures 11. Similarly, some qualitative results for the hearing aid dataset, depicted in Figure 12 make the same point. The errors as expected are distributed around the cut regions: the top and the bottom of the canal, however, the estimated shapes are observed to be in good agreement with the

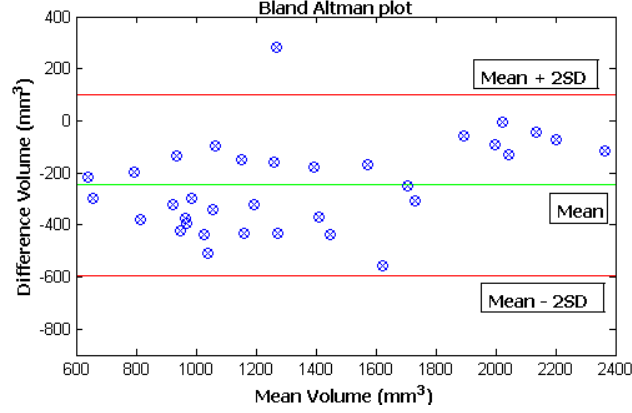


Figure 10: Bland-Altman plot for comparing volume measurements between the GT and the estimated shapes.

GT shapes, particularly in the canal region.

Limitations: In Figure 13, for the pair of shapes (a,b), note that the canal of the patient is short, therefore the top part of the shell was not cut at all. Our algorithm hence could not estimate the cutting plane at the top, and fitted two planes to the bottom. This single cut plane situation can be corrected by detecting the proximity of the estimated planes. Similarly, the experiment in (c,d) shows the importance of correctly estimating the orientation of the cutting plane. With a non-perfect bottom plane as in (d), the resulting shape deformed all the way towards the cutting plane beyond the GT shape. Further improvement on plane estimation could be carried out, however, we suspect that such variations will occur even in cases when a specialist does the detailing twice on the same shell, or even when two different specialists were to design the same person’s shell. However, such data were not available due to high demand, and time-to-market restrictions

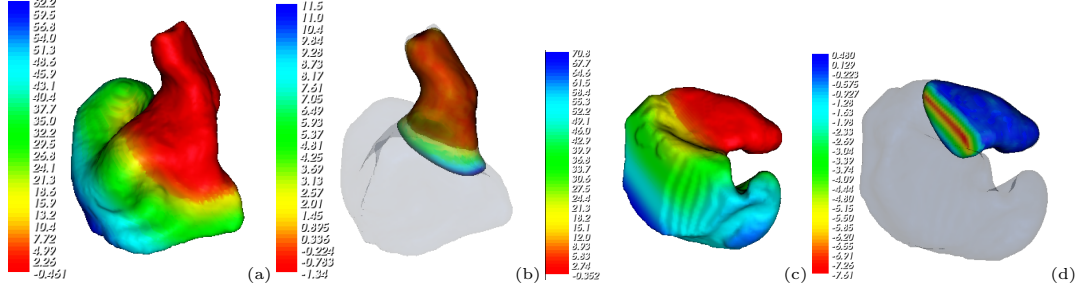


Figure 11: Typical errors in the shape estimation are made in the bottom of the canal due to slight misestimation in the position and orientation of the cutting planes.

in the product line (that is, two different specialists did not work on the same person’s data).

Generally, a good idea to overcome the limitations of a full automatic approach is to devise a hybrid solution where the specialist provides control over the cutting planes, and if necessary intervenes to correct them, as the cutting plane errors seem to be the bottleneck of automatic detailing of hearing aids. As depicted in Figure 14, such an interaction can be inserted into our framework as the steps of shape regression, cut plane estimation, and final morphing constrained by the cut planes are separately executed.

Our experiments demonstrated a proof of concept of the presented method to generate a detailed shell close to that would be produced by a specialist, and good overall performance measures are obtained in all the tests. Further large scale validation is necessary for a rapid prototyping application.

4. Conclusions and Discussions

We presented a general framework to automatically generate a target shape from a reference shape via learning the relation of these two shape

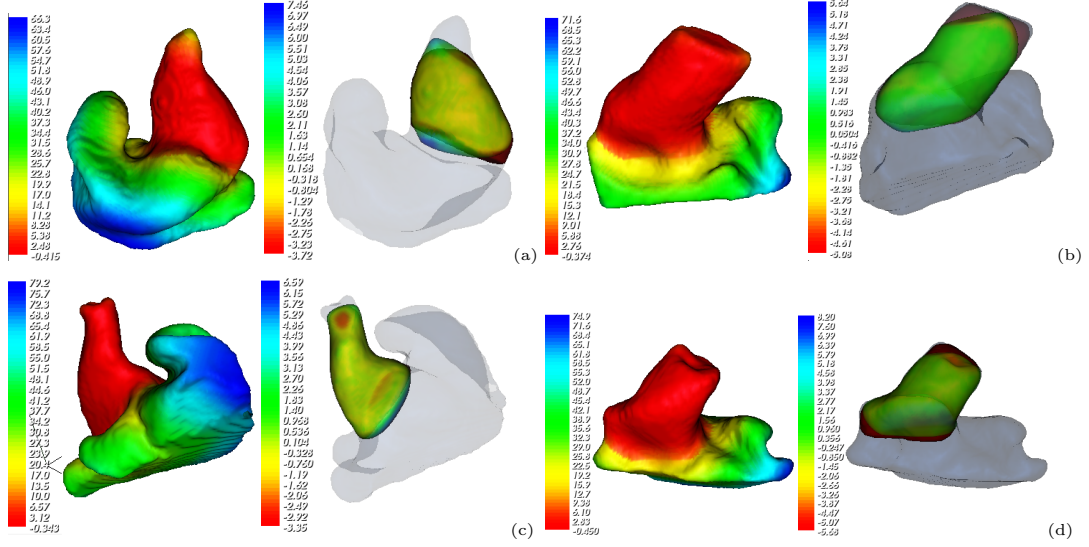


Figure 12: (a,b,c,d) Undetailed input shape (left) and estimated detailed shape with a colormap that depicts the distance to the GT detailed shape which is overlaid over the former two with a transparent dark color.

classes on a much lower dimensional manifold than the original shape space. As a specific application, our system learns how to detail a hearing aid shape by estimating a mapping from a patient’s digitized ear mold to the detailed shell. Further refinement of the shape is achieved by deforming the estimated shell towards the undetailed shell in regions where the shapes should fit using an auxiliary difference shape class. This component could be modeled according to the set of operations and rules required by the specifics of the customized design application. The mapping between two shape classes was estimated through a linear multivariate regression to avoid local nonlinear effects. This framework contains several known components such as variational registration, PCA for shape analysis, and linear regression, however, it is the

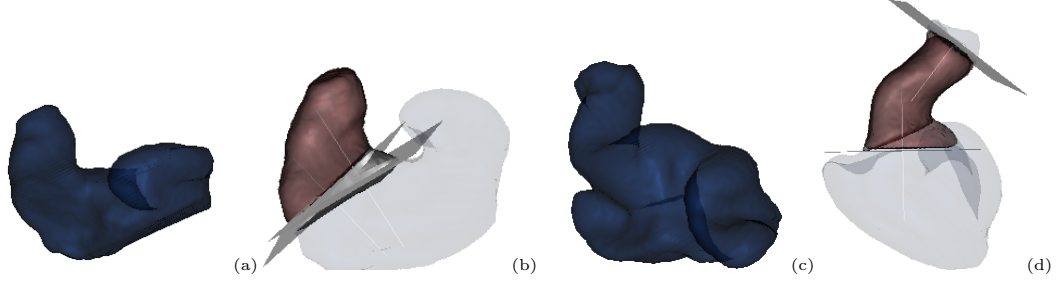


Figure 13: (a,c) Blue/dark the undetailed input shape; (b,d) Light gray GT detailed shape, Red/dark the estimated detailed shape (superimposed on the transparent undetailed shape view). The two estimated cutting planes are also shown.

first time they are combined for a novel automatic shape transformation.

Possible future extensions include replacing some components of this work with other dimensionality reduction techniques such as kernel PCA or normalized PCA. However, a more interesting development involves a nonlinear manifold approach. This is part of our current work, in which the two related shape spaces are modeled via non-parametric probability densities [31] rather than the underlying independent Gaussian probability densities in Eq.(1) which were indirectly coupled via an estimated mapping in this paper. Another direction for improvement of the shape estimation methodology is to use anatomical features or an atlas over the ear impression surfaces to guide the estimation process. Furthermore, various other applications of our technique to custom design of various anatomical parts such as dental implants and prosthetic hips can be specifically designed.

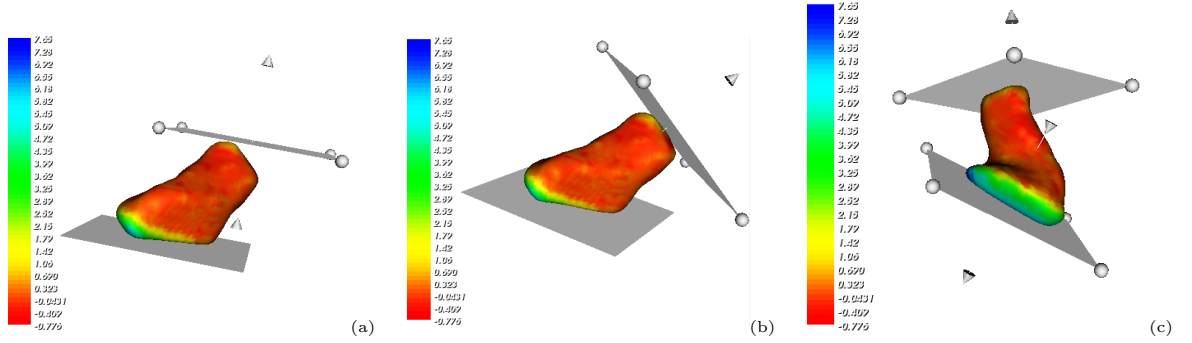


Figure 14: Interaction: Errors in the cut plane orientation estimation in (a) can be corrected by a modification provided by the specialist at the top of the canal in (b), and at the canal bottom in (c).

Acknowledgements

The authors thank Alex Zouhar at Siemens Corporate Research (SCR), Princeton NJ, USA for providing the hearing aid datasets.

- [1] D. Kendall, “Shape manifolds, procrustean metrics and complex projective spaces,” *Bulletin of the London Mathematical Society*, vol. 16, no. 2, pp. 81–121, 1984.
- [2] F. Bookstein, “Size and shape spaces for landmark data in two dimensions,” *Statistical Science*, vol. 1, no. 2, pp. 181–242, 1986.
- [3] I. Dryden and K. Mardia, *Statistical Shape Analysis*. Wiley, Chichester, 1998.
- [4] T. Cootes, C. Taylor, D. Cooper, and J. Graham, “Active shape models - their training and application,” *Computer Vision and Image Understanding*, vol. 61, no. 1, pp. 38–59, January 1995.

- [5] A. Hertzmann, C. Jacobs, N. Oliver, B. Curless, and D. Salesin, “Image analogies,” in *SIGGRAPH Conference Proceedings*, 2001.
- [6] R. Paulsen, R. Larsen, C. Nielsen, S. Laugesen, and B. Ersboll, “Building and testing a statistical shape model of the human ear canal,” in *MICCAI*, 2002, pp. 373–380.
- [7] R. R. Paulsen and K. B. Hilger, “Shape modelling using markov random field restoration of point correspondences,” in *IPMI*, 2003.
- [8] S. Darkner, R. Larsen, and R. Paulsen, “Analysis of deformation of the human ear and canal caused by mandibular movement,” in *MICCAI*, 2007, pp. 801–808.
- [9] M. Leventon, W. Grimson, O. Faugeras, Statistical shape influence in geodesic active contours, in: IEEE Computer Society Conference on Computer Vision and Pattern Recognition, Vol. 1, Hilton Head, 2000.
- [10] Y. Rathi, S. Dambreville, and A. Tannenbaum, “Statistical shape analysis using kernel pca,” in *IS&T, SPIE Symposium on Electronic Imaging*, 2006.
- [11] D. Cremers and T. Kohlberger, “Probabilistic kernel PCA and its application to statistical shape modeling and inference,” in *Kernel Methods in Bioengineering, Signal and Image Processing*, G. C.-V. et al., Ed. Idea Group Inc., 2006.
- [12] M. Aguirre, M. Linguraru, K. Marias, N. Ayache, L.-P. Nolte, and M. Ballester, “Statistical shape analysis via principal factor analysis,” in *IEEE Int. Symp. Biomedical Imaging*, 2007.

- [13] A. Rao, P. Aljabar, and D. Rueckert, “Hierarchical statistical shape analysis and prediction of sub-cortical brain structures,” *Medical Image Analysis*, vol. 12, 2008.
- [14] B. Davis, P. Fletcher, E. Bullitt, and S. Joshi, “Populations shape regression from random design data,” in *IEEE Int. Conf. Computer Vision*, 2007.
- [15] H. Gray, “Gray’s anatomy of the human body,” in www.bartleby.com/107/229.html, 1918.
- [16] M. Kilian, N. J. Mitra, and H. Pottmann, “Geometric modeling in shape space,” *ACM Trans. Graphics*, vol. 26, no. 3, 2007, Proc. SIGGRAPH.
- [17] G. Slabaugh, T. Fang, F. McBagonluri, A. Zouhar, R. Melkisetoglu, H. Xie, and G. Unal, “3d shape modeling for hearing aid design,” *IEEE Signal Processing Magazine*, pp. 98–102, September 2008.
- [18] N. Paragios, M. Rousson, and V. Ramesh, “Distance transforms for non-rigid registration,” *Computer Vision and Image Understanding (CVIU)*, vol. 89, no. 2-3, pp. 142–165, February-March 2003.
- [19] G. H. Golub, C. F. Van Loan, *Matrix Computations*. The Johns Hopkins University Press, 1996.
- [20] Weingarten, J., Gruener, G., and R. Siegwart, “Probabilistic plane fitting in 3d and an application to robotic mapping,” in *Proceedings of ICRA 2004*, 2004.

- [21] J. Sethian, *Level Set Methods and Fast Marching Methods*. Cambridge University Press, 1999.
- [22] R. T. Whitaker and D. E. Breen, “Level-set models for the deformation of solid objects,” in *InEurographics/Siggraph, Proceedings of Implicit Surfaces*, 1998, pp. 19–35.
- [23] M. Turk, A. Pentland, Eigenfaces for recognition, *Journal of Cognitive Neuroscience* 3 (1) (1991) 71–86.
- [24] D. Anguelov, P.Srinivasan, D.Koller, S.Thrun, J. Rodgers, J.Davis, SCAPE: Shape completion and animation of people, in: *Proceedings of the SIGGRAPH Conference*, 2005.
- [25] B. Allen, B. Curless, Z. Popović, The space of human body shapes: reconstruction and parameterization from range scans, in: *ACM SIGGRAPH 2003*, pp. 587–594.
- [26] S. Rusinkiewicz, M. Levoy, Efficient variants of the ICP algorithm, in: *The IEEE Int. Wkshp on 3-D Digital Imaging and Modeling (3DIM)*, 2001, pp. 145–152.
- [27] A. Zouhar, T. Fang, G. Unal, G. Slabaugh, H. Xie, F. McBagonluri, Anatomically-aware, automatic, and fast registration of 3d ear impression models, *Third International Symposium on 3D Data Processing, Visualization and Transmission (3DPVT)*.
- [28] P. Besl, N. McKay, A method for registration of 3-D shapes, *IEEE Trans. Pattern Analysis and Machine Intelligence* 14 (1992) 239–256.

- [29] I.L. Dryden, Statistical shape analysis in archaeology, Spatial Statistics in Archaeology Workshop, 2000.
- [30] D.G. Altman, J.M. Bland, Measurement in Medicine: The Analysis of Method Comparison Studies, Journal of the Royal Statistical Society, Vol. 32, no. 3, 1983, pp. 307–317.
- [31] G. Unal, Nonparametric Joint Shape Learning for Customized Shape Modeling, Computerized Medical Imaging and Graphics, Vol. 34, no. 4, 2010, pp. 298–307.